Waves cue distinct behaviors and differentiate transport of congeneric snail larvae from sheltered versus wavy habitats

Heidi L. Fuchs[1*], **Gregory P. Gerbi**[2], **Elias J. Hunter**[1], and **Adam J. Christman**[1]

[1]Rutgers University, New Brunswick, New Jersey 08901

[2]Skidmore College, Saratoga Springs, New York 12866

*Corresponding author. Email: hfuchs@marine.rutgers.edu

Supporting Information: Appendix

Methods: Standard Error of Threshold Estimates

Figure 2 shows behavior thresholds x_{cr}, which were estimated as $\log_{10}(x_{cr}) = (a_0 - a_1)/a_2$ from the piecewise model fit (Eq. 1), and their standard errors. The standard errors $\sigma_{\log_{10}(x_{cr})}$ were computed from variances and covariances of the parameter estimates a_i. Because $\log_{10}(x_{cr})$ is a derived parameter, we used the Taylor series approximation for the variance of $f = (a_0 - a_1)/a_2$,

$$
\sigma_f^2 = \left(\frac{\partial f}{\partial a_0}\right)^2 \sigma_{a_0}^2 + \left(\frac{\partial f}{\partial a_1}\right)^2 \sigma_{a_1}^2 + \left(\frac{\partial f}{\partial a_2}\right)^2 \sigma_{a_2}^2 + 2\left(\frac{\partial f}{\partial a_0}\right)\left(\frac{\partial f}{\partial a_1}\right)\mathrm{cov}(a_0, a_1) + \ldots
$$
$$
2\left(\frac{\partial f}{\partial a_0}\right)\left(\frac{\partial f}{\partial a_2}\right)\mathrm{cov}(a_0, a_2) + 2\left(\frac{\partial f}{\partial a_1}\right)\left(\frac{\partial f}{\partial a_2}\right)\mathrm{cov}(a_1, a_2)
$$

(S1)

(e.g., 1), where

$$
\frac{\partial f}{\partial a_0} = \frac{1}{a_2}, \quad \frac{\partial f}{\partial a_1} = -\frac{1}{a_2}, \quad \frac{\partial f}{\partial a_2} = \frac{a_1 - a_0}{a_2^2}. \tag{S2}
$$

In addition, $\mathrm{cov}(a_0, a_1) = \mathrm{cov}(a_0, a_2) = 0$ because the two linear pieces of the model are independent of each other (Eq. 1). Combining these relationships, the variance of $\log_{10}(x_{cr})$ is

$$
\sigma_{\log_{10}(x_{cr})}^2 = \frac{1}{a_2^4}\left[a_2^2\left(\sigma_{a_0}^2 + \sigma_{a_1}^2\right) + \sigma_{a_2}^2\left(a_0 - a_1\right)^2 + 2\left(a_0 - a_1\right)a_2\mathrm{cov}(a_1, a_2)\right]. \tag{S3}
$$

Methods: Environmental Data Analysis

Physical data were synthesized from buoy observations in locations harboring adult populations of *T. obsoleta* (Delaware Bay) and *T. trivittata* (New Jersey shelf) and from a previously published 3-dimensional hydrodynamic model (2) encompassing both habitats (Fig. 1). Analyses are based on the assumptions that turbulence is isotropic (statistically invariant with rotation) at larval scales (e.g., 3), waves are linear (e.g., 4), and turbulence and wave motions are independent and additive (e.g., 5). In Delaware Bay, turbulence is mainly tide-generated and waves are smaller, whereas on the NJ shelf, near-surface turbulence is mainly wind-generated and waves can be large. We characterized these representative habitats of *T. obsoleta* and *T. trivittata*, respectively, by computing turbulence- and wave-generated signals and quantifying their frequency distributions in the water column and bottom boundary layer (BBL).

Turbulence-generated signals were computed using the hydrodynamic model, which lacked waves but had realistic winds and heating on a grid spanning Delaware Bay and the adjacent shelf (2). Daily model outputs from 1 April to 1 September 2010 were subdivided into estuary and shelf subsections (Fig. 1). For the water column, we used the upper 75% of model levels; on the shelf, this upper region had mainly wind-generated turbulence with little influence from the bottom boundary layer. For the BBL, we used the bottom model level, where heights above bottom ranged from 0.05 to 0.7 m. Dissipation rates $\varepsilon_{\text{model}}$ were computed from model outputs (6; 7) and were then used to calculate turbulence-generated vorticity SD and acceleration SD (8).

Wave-generated signals were computed from buoy data. For Delaware Bay, we used wave data from a short-term Waverider buoy deployment (25 March to 3 August 2014). For the New Jersey shelf, we used eight years (2009-2016) of archived wind and wave data from two National Data Buoy Center discus buoys (44009 and 44065). Wave-generated acceleration SD were estimated using the significant wave heights and dominant wave periods, assuming that most energy is in motions at the dominant frequency (8). The shelf buoy data include wind speed, so we also estimated concurrent turbulence-generated signals – vorticity SD and acceleration SD – from the dissipation rate computed as $\varepsilon_{\text{wind}} = u_*^3 (\kappa z)^{-1}$, where u_* is shear velocity derived from the wind speed (8) and $\kappa = 0.4$ is von Karman's constant. All signals were computed at 10 cm depth increments over the water column (upper 75%), and wave-generated signals were computed in the BBL (0.5 m above bottom).

We combined model and buoy data at two locations (Delaware Bay wave buoy and 44009 on the shelf) to estimate the typical ranges of co-occurring total acceleration and vorticity in the two species' habitats. Signals were computed for the water column and BBL as described above. For the shelf water column, we used the co-occurring turbulence- and wave-generated signals estimated from concurrent wind and wave data from the buoy (44009). For all other locations, we combined wave-generated accelerations from buoy data and turbulence-generated signals from model outputs at the grid point nearest each buoy.

The model and buoy datasets were not concurrent, so we used a Monte Carlo simulation to estimate the joint frequency of total signals. For the Delaware Bay water column, model dissipation rates $\varepsilon_{\text{model}}$ were first interpolated to the 10 cm depth increments used for wave analysis. For the BBL in both habitats, we used the bottom model level and wave analysis at 0.5 m above bottom. At each depth z, we randomly generated $N = 500$ dissipation rates from an extreme value distribution fitted to

3

$\log_{10} \varepsilon_{\mathrm{model}}(z)$. Although dissipation rates often have a lognormal distribution (e.g., 9), a Lilliefors test rejected that distribution for the BBL and parts of the water column where $\log_{10} \varepsilon$ were highly asymmetric (Fig. 5), and the extreme value distribution gave a better fit. From these simulated dissipation rates, we computed the turbulence-generated signals and then recombined each simulated profile with each wave-generated acceleration profile from every time point of the buoy record to generate co-occurring turbulence- and wave-generated signals with appropriate joint frequencies. Acceleration variances from the two sources were summed to estimate total acceleration SD. The co-occurring total signals are representative of the conditions experienced by larvae in the water column and BBL of inlets and estuaries (*T. obsoleta* habitat) and over the shelf (*T. trivittata*).

Table S1: Summary of average flow statistics in turbulence tank. Level indicates turbulence tank setting, f is stirring grid oscillation frequency, W is mean vertical velocity (positive upwards), $w_{\mathrm{RMS}}/u_{\mathrm{RMS}}$ is isotropy ratio, ε is dissipation rate, η_k is Kolmogorov length scale, λ is Taylor microscale, and Δx is PIV vector resolution.

level	f	W	$w_{\mathrm{RMS}}/u_{\mathrm{RMS}}$	ε	η_k	λ	Δx
	(Hz)	cm s^{-1}		(cm^2 s^{-3})	(cm)	(cm)	(cm)
0.4	0.14	0.05	1.38	4.7×10^{-5}	0.39	2.71	0.21
0.6	0.17	0.07	1.54	1.4×10^{-3}	0.19	1.60	0.14
1.0	0.42	0.19	1.05	7.1×10^{-3}	0.11	1.20	0.07
2.0	0.98	0.48	0.98	2.2×10^{-1}	0.05	0.57	0.03
3.0	1.56	0.65	1.00	8.2×10^{-1}	0.03	0.48	0.03

Table S2: Summary of larval measurements associated with experiments in each flow tank. Tank orientations (H, horizontal; V, vertical) are indicated for simple flows. Includes species, larval competency status (PC, precompetent; C, competent), and number of replicates for each group. Larval ages given as ranges. Larval concentrations, shell lengths (d), terminal sinking velocities (w_T), and specific densities (ρ_p) given as means ± 1 SD over replicates. Terminal velocities from videos of sinking dead larvae; densities estimated using Rubey's modification of Stokes' Law (10; 11). Behavioral vertical velocity (w_b), propulsive force magnitude ($|\mathbf{F}_v|$), and % of larvae swimming given as mean ± 1 SD of observations in still water; results shown for the three experiments with the most still-water observations per larval group.

flow tank	species (competency)	reps #	concentration # larvae L^{-1}	age d	d μm	w_T cm s^{-1}	ρ_p g cm^{-3}	w_b cm s^{-1}	$|\mathbf{F}_v|$ ×10^{-8} N	swim %
Turbulence	*T. obsoleta* (PC)	2	150 ± 0	7	362 ± 18	-0.36 ± 0.2	1.08 ± 0.04			
	T. obsoleta (C)	4	40 ± 41	23–26	621 ± 58	-0.51 ± 0.1	1.05 ± 0.01	0.003 ± 0.10	3.4 ± 0.7	100
	T. trivittata (C)	2	75 ± 35	22–23	662 ± 22	-0.51 ± 0.07	1.05 ± 0.0	-0.01 ± 0.10	3.8 ± 0.8	100
Couette (H)	*T. obsoleta* (PC)	2	500 ± 0	7–8	319 ± 10	-0.28 ± 0.0	1.08 ± 0.0			
	T. obsoleta (C)	3	770 ± 150	24–27	655 ± 120	-0.56 ± 0.16	1.05 ± 0.01			
Couette (V)	*T. obsoleta* (PC)	2	1100 ± 210	7–8	307 ± 1	-0.28 ± 0.03	1.09 ± 0.01			
	T. obsoleta (C)	3	600 ± 170	24–28	691 ± 96	-0.57 ± 0.8	1.05 ± 0.0			
Cylinder (H)	*T. obsoleta* (PC)	2	900 ± 0	8–9	389 ± 11	-0.30 ± 0.01	1.06 ± 0.0	0.03 ± 0.06	1.3 ± 0.3	100
	T. obsoleta (C)	2	450 ± 350	24–25	588 ± 28	-0.38 ± 0.07	1.05 ± 0.01			
	T. trivittata (C)	2	100 ± 0	24–25	694 ± 1	-0.61 ± 0.03	1.06 ± 0.01			
Cylinder (V)	*T. obsoleta* (PC)	2	900 ± 0	6–7	365 ± 1	-0.31 ± 0.02	1.07 ± 0.0			
	T. obsoleta (C)[1]	2	200 ± 0	25–26	721 ± 1	-0.68 ± 0.09	1.1 ± 0.01			
Shaker (H)	*T. obsoleta* (PC)	2	600 ± 280	7–10	384 ± 47	-0.29 ± 0.01	1.07 ± 0.01	0.03 ± 0.07	1.3 ± 0.3	100
	T. obsoleta (C)	2	1000 ± 280	25	674 ± 13	-0.70 ± 0.11	1.08 ± 0.01	0.01 ± 0.15	5.8 ± 1.7	100
	T. trivittata (C)	3	730 ± 310	21–26	739 ± 124	-0.59 ± 0.07	1.05 ± 0.01	-0.02 ± 0.16	4.5 ± 1.9	99
Shaker (V)	*T. obsoleta* (PC)	2	2000 ± 0	7–8	344 ± 28	-0.28 ± 0.01	1.07 ± 0.0	0.007 ± 0.04	1.1 ± 0.2	100
	T. obsoleta (C)	2	700 ± 140	25	639 ± 0	-0.62 ± 0.21	1.06 ± 0.01	-0.02 ± 0.16	5.3 ± 1.7	100
	T. trivittata (C)	2	1500 ± 0	24–25	901 ± 29	-0.49 ± 0.05	1.04 ± 0.01	-0.04 ± 0.18	3.9 ± 2.3	95

[1]PIV data not analyzed due to poor image quality.

Table S3: Threshold signals (x_{cr}) and coefficients of determination (R^2) from piecewise linear regressions (Eq. 3 in text) of behavior metrics versus physical signals. Larval developmental stages indicated as precompetent (PC) or competent (C), vertical brackets indicate magnitude, n.s. indicates that linear regressions were not significant, and n.t. indicates that piecewise regression identified no threshold within the data range.

| flow tank	signal (units)	behavior metric	*T. obsoleta* (PC)		*T. obsoleta* (C)		*T. trivittata* (C)	
			x_{cr}	R^2	x_{cr}	R^2	x_{cr}	R^2
turbulence	ε	fraction swimming	1.2×10^{-5}	0.78	2.0×10^{-5}	0.37	5.6×10^{-6}	0.57
	(m^2 s^{-3})	$|\mathbf{F_v}|$ swimming	5.0×10^{-5}	0.06	4.0×10^{-5}	0.47	7.6×10^{-6}	0.69
		$|\mathbf{F_v}|$ sinking/diving	n.t.	0.26	1.9×10^{-4}	2.7×10^{-3}	n.s.	n.s.
cylinder (horiz.)	$|\xi|$	fraction swimming	0.47	0.56	1.1	0.41	2.8	0.73
	(s^{-1})	$|\mathbf{F_v}|$ swimming	1.0	0.88	1.7	0.96	2.4	0.79
		$|\mathbf{F_v}|$ sinking/diving	2.3	0.45	n.t.	0.20	n.t.	0.45
shaker (horiz.)	$|\alpha|$	fraction swimming	1.6×10^{-1}	0.53	n.s.	n.s.	8.7×10^{-2}	0.93
	(m s^{-2})	$|\mathbf{F_v}|$ swimming	1.1×10^{-1}	0.79	1.8×10^{-1}	0.86	6.4×10^{-2}	0.99
		$|\mathbf{F_v}|$ sinking/diving	2.0×10^{-3}	0.44	n.s.	n.s.	2.9×10^{-2}	0.71
shaker (vert.)	$|\alpha|$	fraction swimming	1.2×10^{-1}	0.62	2.2×10^{-1}	0.98	9.5×10^{-3}	0.50
	(m s^{-2})	$|\mathbf{F_v}|$ swimming	1.6×10^{-1}	0.93	n.s.	n.s.	8.6×10^{-2}	0.97
		$|\mathbf{F_v}|$ sinking/diving	3.7×10^{-2}	0.48	n.s.	n.s.	9.7×10^{-2}	0.84
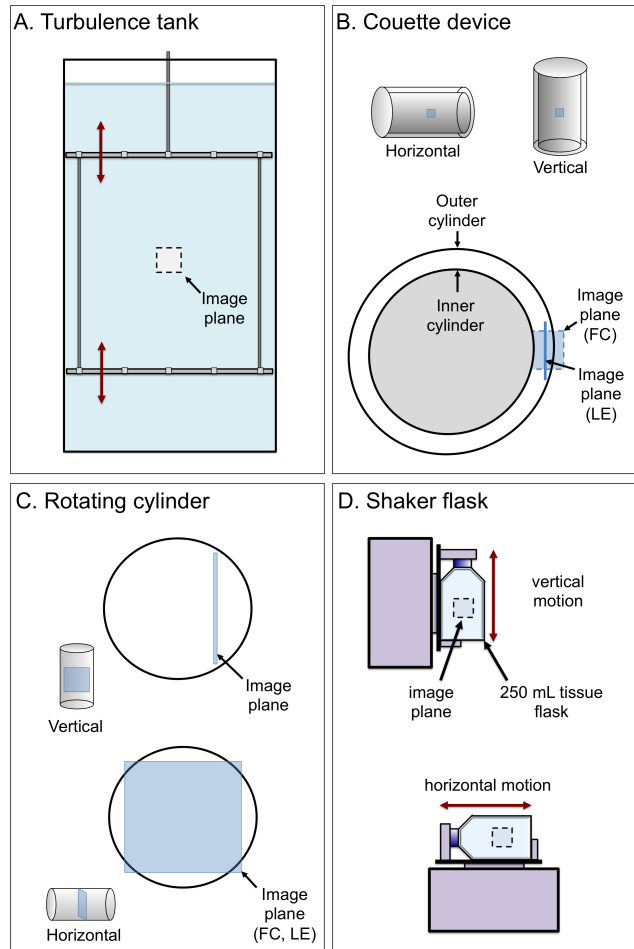
Figure S1: Diagram of flow tanks and image locations. Turbulence tank (A) has a grid mesh size of $M = 8.25$ cm, a grid separation distance of $H = 45.7$ cm, a peak-to-peak grid stroke distance of $S = 8.89$ cm, and a 6.6 cm wide image plane. Couette device (B) has a 7.6 cm inner cylinder radius, a 9.5 cm outer cylinder radius, and a 3.2 cm wide image plane. Rotating cylider (C) has a 4.8 cm radius and a 7.5 cm wide image plane. Shaker flask (D) has a 2 cm peak-to-peak oscillation amplitude and a 5 cm wide image plane. In cylindrical tanks (B,C), flow characterizations were done using planes perpendicular to long axis (FC). Larval experiments (LE) were done using lateral image planes parallel to long axis, except in horizontally rotating cylinder (C), and out-of-plane motions were estimated from flow characterizations (12). Couette device, rotating cylinder, and shaker flask redrawn from Fuchs et al. (12; 13). Videos online at http://marine.rutgers.edu/~hfuchs/BPI_Lab/flow-tanks.html.
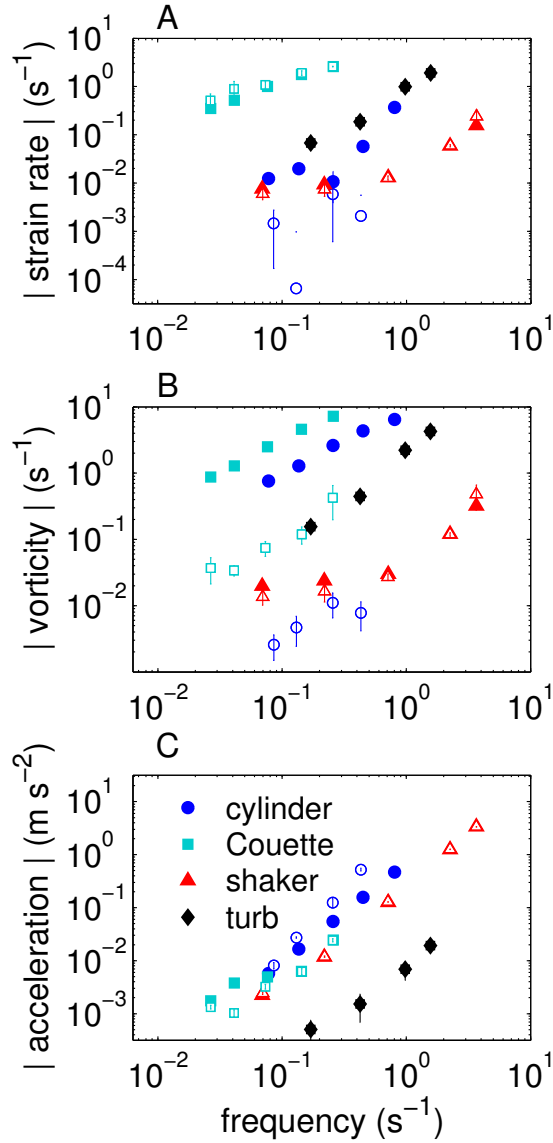
Figure S2: Summary of hydrodynamic signals in turbulence tank and in simple flow tanks. Includes strain rate γ (A), horizontal (tilt-inducing) component of vorticity ξ (B), and centripetal or linear acceleration α (C) versus average rotation or oscillation frequency f. Symbols for turbulence are mean ± 1 SE over replicates of the signal standard deviations in grid-stirred turbulence. Symbols for simple flows are mean ± 1 SE over replicates of the time- and space-averaged signal in the cylinder (vorticity-dominated flow, blue circles) rotating about a horizontal (closed circles) or vertical axis (open circles), the Couette device (strain-dominated flow; cyan squares) rotating about a horizontal (closed squares) or vertical axis (open squares), and the shaker flask (acceleration-dominated flow; red triangles) oscillating horizontally (closed triangles) or vertically (open triangles). Some symbols overlap.

9
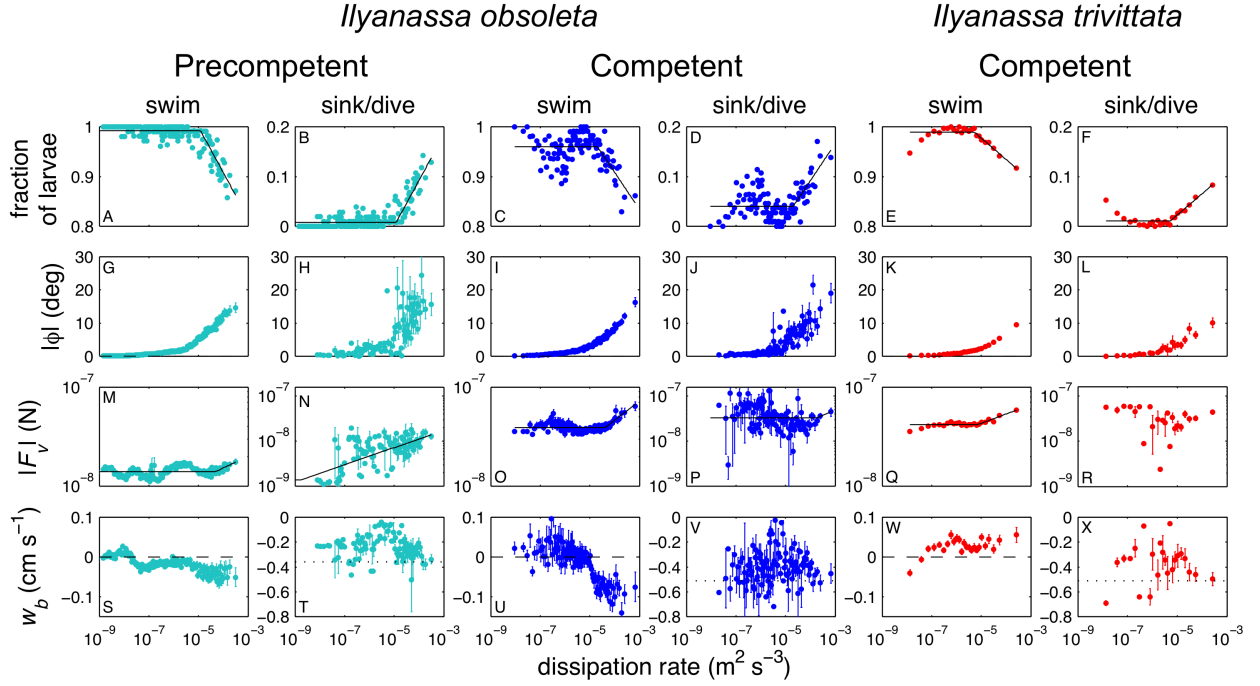
Figure S3: Responses of snail larvae to grid-stirred turbulence. Results for precompetent (cyan) and competent (blue) *T. obsoleta* and competent *T. trivittata* (red) shown separately for larvae propelling themselves upward (swimming) and downward (sinking/diving), including fraction of larvae with each behavior (A–F), flow-induced tilt angle magnitude ($|\phi|$; G–L), larval propulsive force magnitude ($|\mathbf{F_v}|$; M–R), and vertical velocity due to behavior (w_b; S–X) versus dissipation rate. Replicates are pooled, symbols are means ± 1 SE of instantaneous estimates in small bins of dissipation rate ($N = 100$), dashed lines indicate neutral buoyancy ($w_b = 0$), and dotted lines indicate terminal sinking velocity ($w_b = w_T$). Solid lines (A–F, M–R) are piecewise linear regressions (Eq. 1) used to identify threshold signals inducing propulsive reactions if linear regressions were significant at $\alpha = 0.05$.
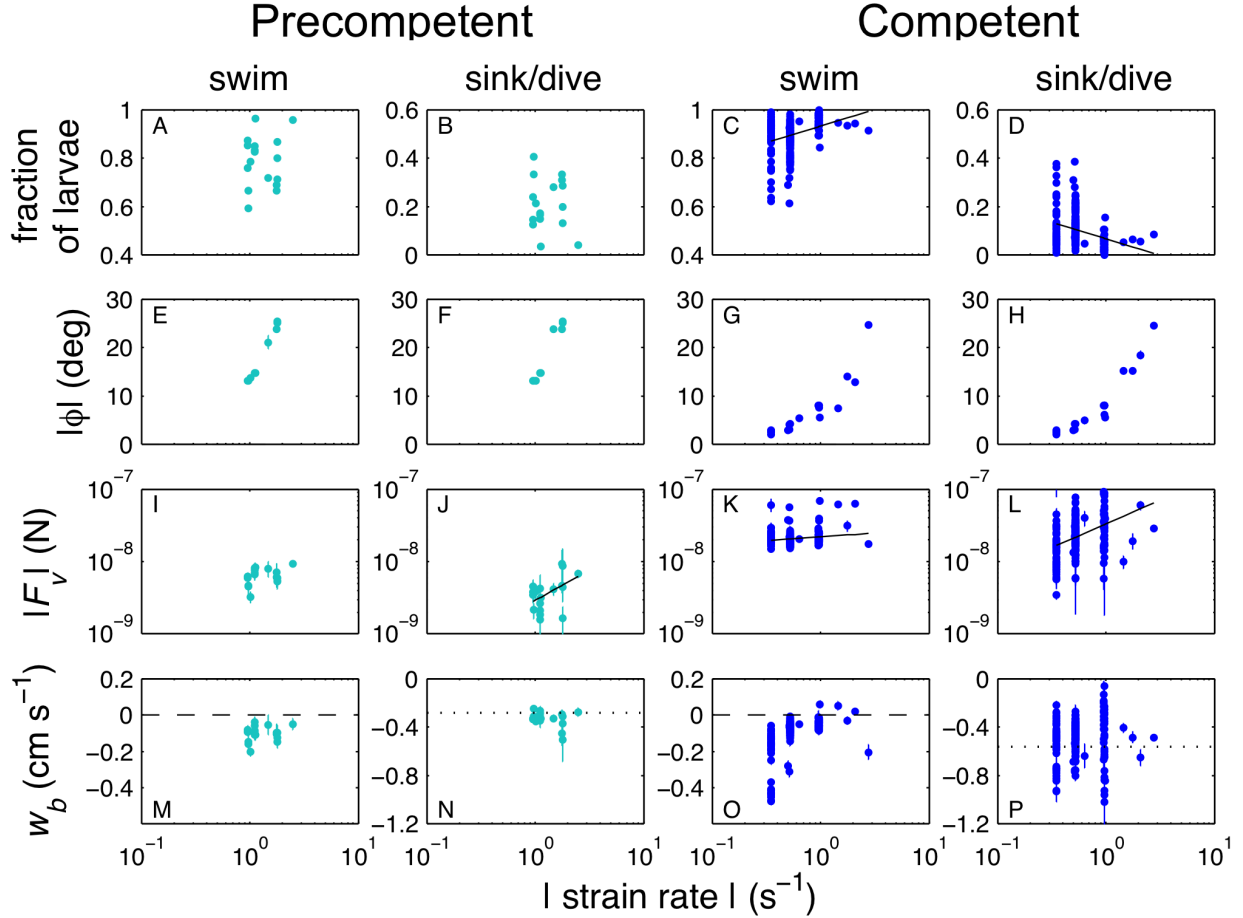
Figure S4: Responses of snail larvae to strain rate in the Couette device rotating about a horizontal axis, where flow would be sensed as a combination of fluid deformation and vorticity-induced tilting. Results for precompetent (cyan) and competent (blue) *T. obsoleta* are shown separately for larvae propelling themselves upward (swimming) and downward (sinking/diving) and include the fraction of larvae in each behavior (A–D), flow-induced tilt angle magnitude (E–H), larval propulsive force (I–L), and vertical velocity due to behavior (M–P) versus strain rate. Symbols and lines as in Fig. S3 with bins of $N = 20$ for precompetent larvae and $N = 100$ for competent larvae. Solid lines (J-L) are linear regression ($\log_{10}$-$\log_{10}$ scale) significant at $\alpha = 0.05$; no thresholds were identified by the piecewise model.
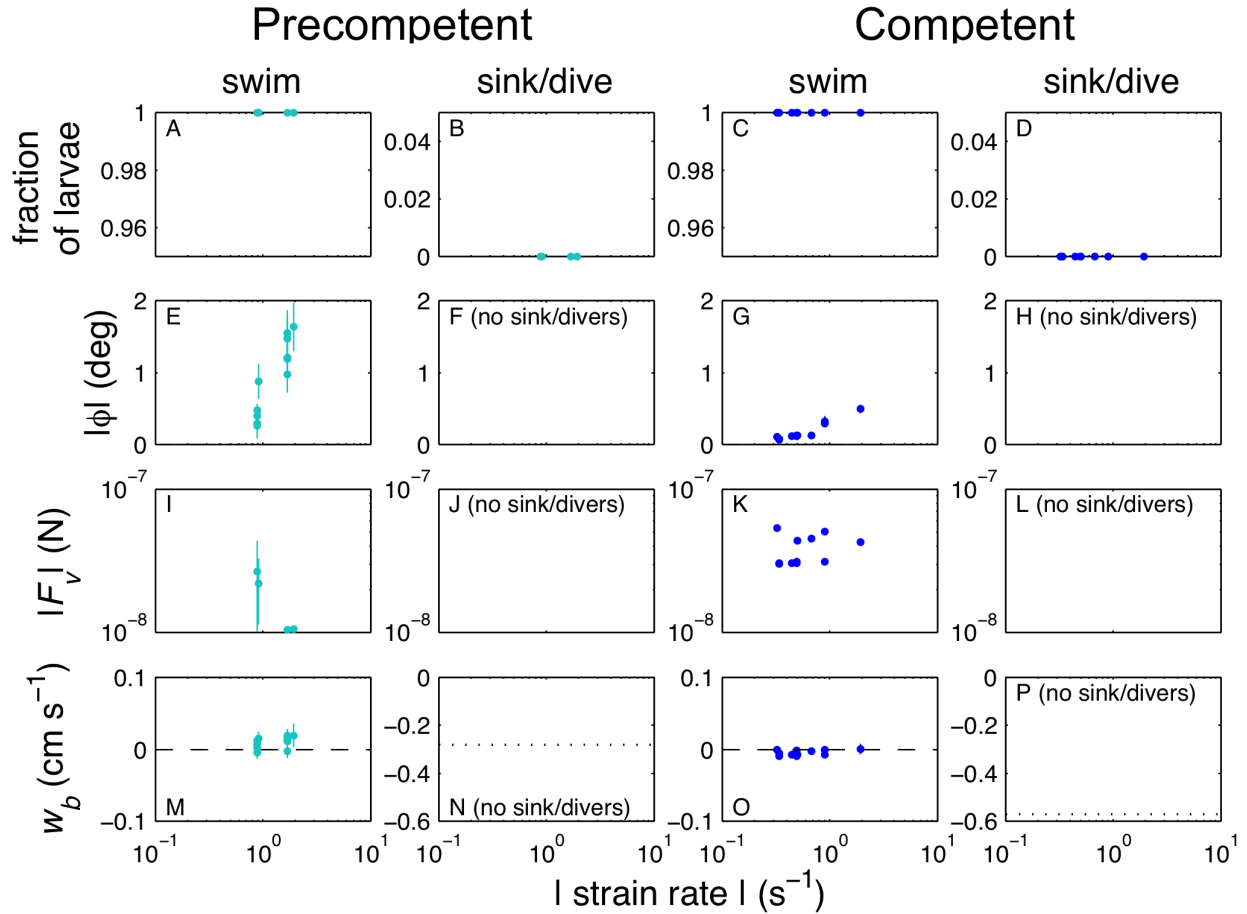
Ilyanassa obsoleta

Figure S5: Responses of snail larvae to strain rate in the Couette device rotating about a vertical axis, where flow would be sensed primarily by velar cilia as fluid deformation. Results for precompetent (cyan) and competent (blue) *T. obsoleta* are shown separately for larvae propelling themselves upward (swimming) and downward (sinking/diving) and include the fraction of larvae in each behavior (A–D), flow-induced tilt angle magnitude (E–H), larval propulsive force (I–L), and vertical velocity due to behavior (M–P) versus strain rate. Symbols and lines as in Fig. S3 with $N = 20$ for precompetent larvae and $N = 100$ for competent larvae. Solid line in K is linear regression ($\log_{10}$-$\log_{10}$ scale) significant at $\alpha = 0.05$; no other regressions were significant for this flow condition.
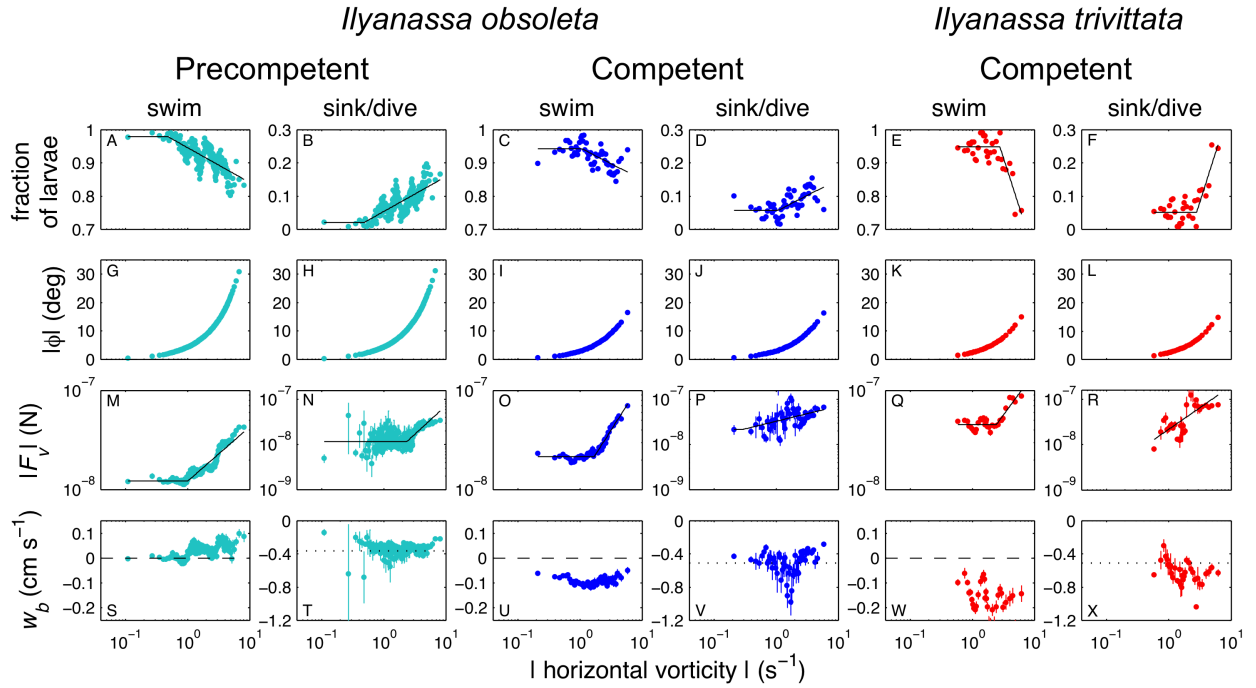
12

Figure S6: Responses of snail larvae to vorticity-dominated flow in cylinder rotating about a horizontal axis, where flow would be sensed primarily by statocysts as tilting relative to gravity. Results for precompetent (cyan) and competent (blue) *T. obsoleta* and competent *T. trivittata* (red) shown separately for larvae propelling themselves upward (swimming) and downward (sinking/diving), including fraction of larvae with each behavior (A–F), flow-induced tilt angle magnitude ($|\phi|$; G–L), larval propulsive force magnitude ($|\mathbf{F_v}|$; M–R), and vertical velocity due to behavior (w_b; S–X) versus horizontal component of vorticity. Symbols and lines as in Fig. S3 with bins of $N = 300$ for *T. obsoleta* and $N = 100$ for *T. trivittata*.
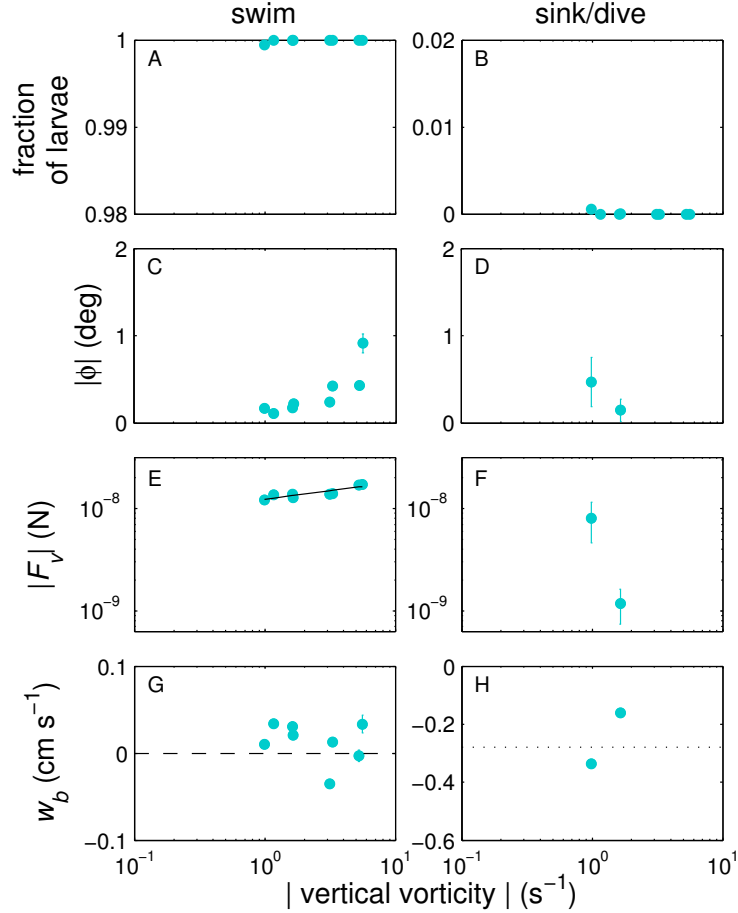
Figure S7: Responses of precompetent *T. obsoleta* larvae to vorticity in the cylinder rotating about a vertical axis, where flow would induce larvae to spin but not tilt. Results are shown separately for larvae propelling themselves upward (swimming) and downward (sinking/diving) and include the fraction of larvae in each behavior (A–B), flow-induced tilt angle magnitude (C–D), larval propulsive force (E–F), and vertical velocity due to behavior (G–H) versus vertical vorticity. Symbols are means ± 1 SE for instantaneous estimates in bins of theoretical vorticity ($= 4\pi f$; one symbol per replicate). Lines as in Fig. S3. Solid line in E is a linear regression ($\log_{10}$-$\log_{10}$ scale) significant at $\alpha = 0.05$; no other regressions were significant for this flow condition.
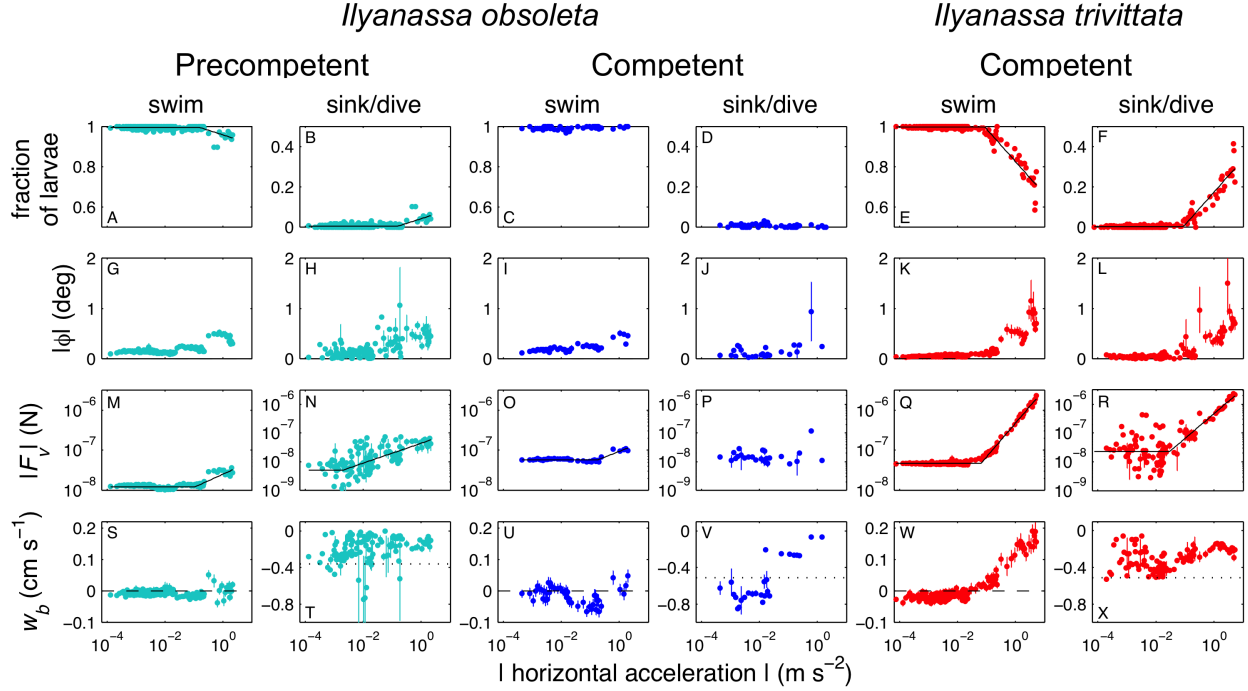
Figure S8: Responses of snail larvae to rectilinear acceleration in shaker flask oscillating horizontally, where flow would be sensed primarily by statocysts as side-to-side acceleration. Results for precompetent (cyan) and competent (blue) *T. obsoleta* and competent *T. trivittata* (red) shown separately for larvae propelling themselves upward (swimming) and downward (sinking/diving), including fraction of larvae with each behavior (A–F), flow-induced tilt angle magnitude ($|\phi|$; G–L), larval propulsive force magnitude ($|\mathbf{F_v}|$; M–R), and vertical velocity due to behavior (w_b; S–X) versus horizontal acceleration. Symbols and lines as in Fig. S3 with bins of $N = 100$.
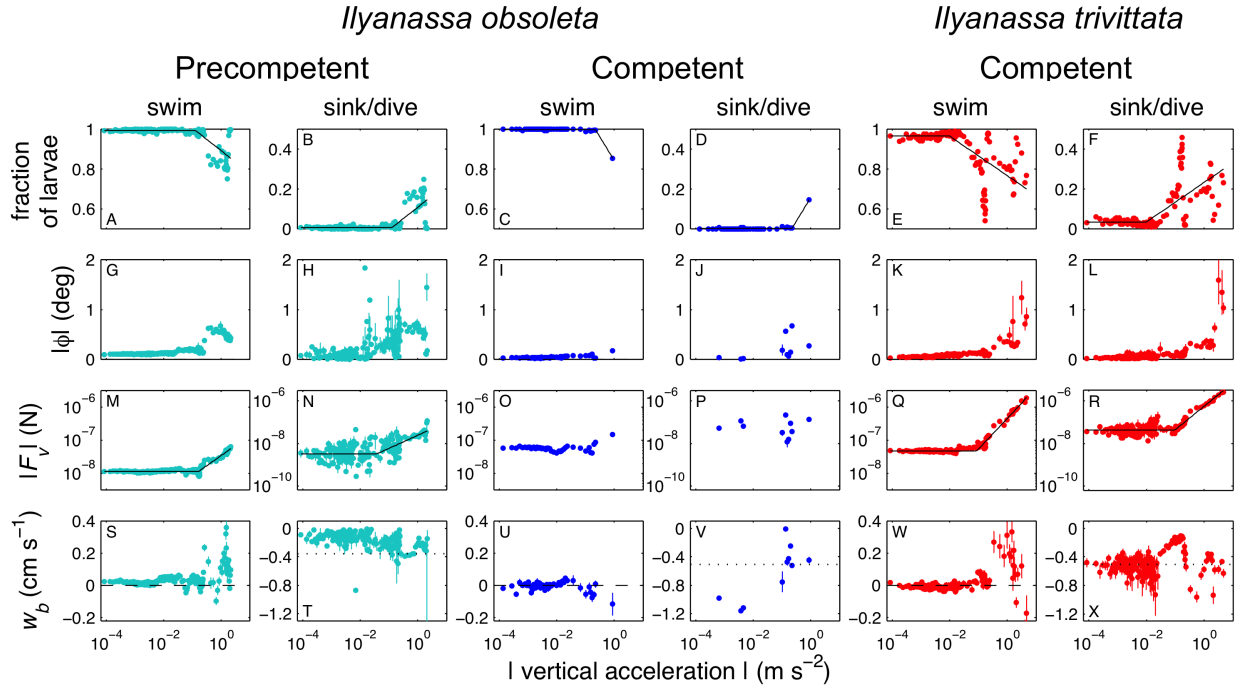
Figure S9: Responses of snail larvae to rectilinear acceleration in the shaker flask oscillating vertically, where flow would be sensed primarily by the statocysts as top-to-bottom acceleration. Results for precompetent (cyan) and competent (blue) *T. obsoleta* and competent *T. trivittata* (red) are shown separately for larvae propelling themselves upward (swimming) and downward (sinking/diving) and include the fraction of larvae in each behavior (A–F), flow-induced tilt angle magnitude (G–L), larval propulsive force (M–R), and vertical velocity due to behavior (S–X) versus vertical acceleration. Symbols and lines as in Fig. S3 with bins of $N = 100$ for competent *T. obsoleta* and $N = 300$ for precompetent *T. obsoleta* and *T. trivittata*.
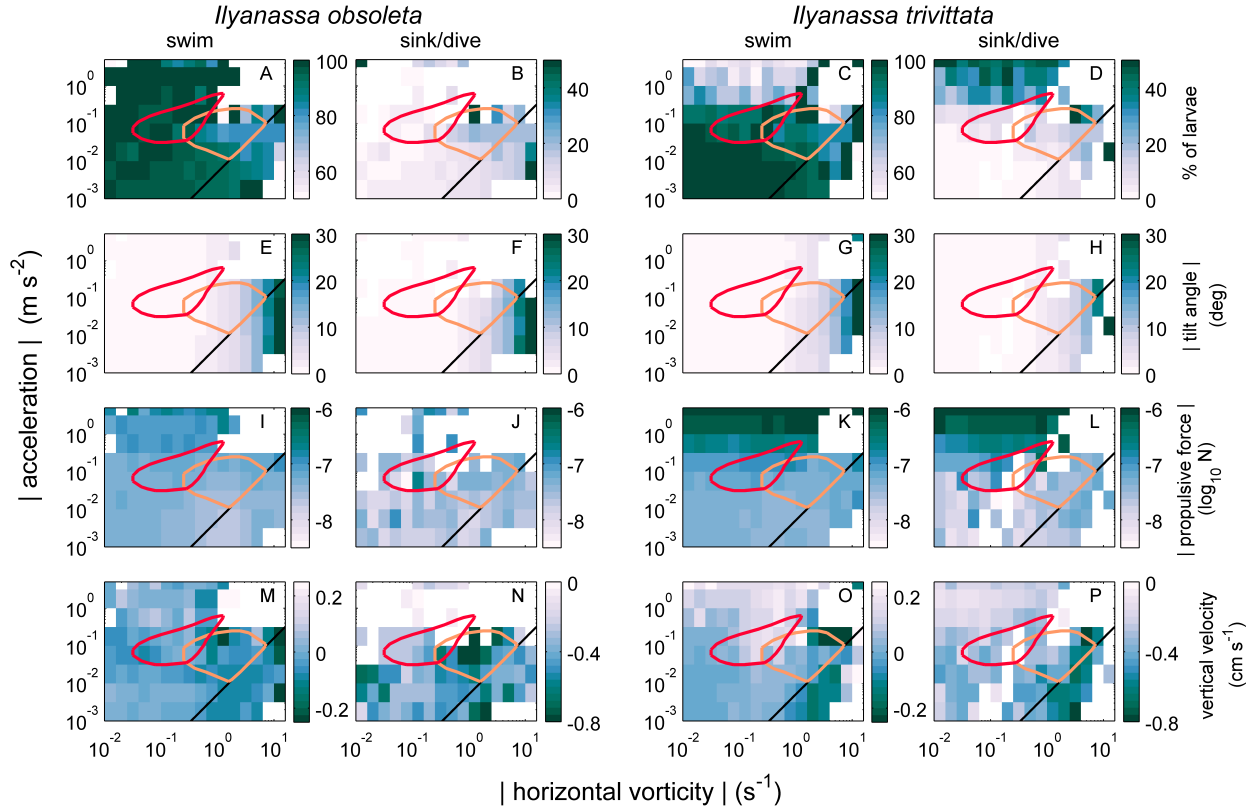
Figure S10: Behavior of competent inlet larvae (*T. obsoleta*; left) and shelf larvae (*T. trivittata*; right) as a function of turbulence- and wave-generated signals with reference to signals typical of their adult habitats. Observed larval swimming and sinking/diving behavior shown versus instantaneous magnitudes of fluid acceleration α and horizontal vorticity ξ. Includes percentage of larvae performing each behavior (A–D), flow-induced tilt angle magnitude ($|\phi|$; E–H), propulsive force magnitude ($|\mathbf{F_v}|$, I–L), and behavioral vertical velocity w_b (M–P). Instantaneous observations of larval velocity are combined from multiple experiments and averaged over bins of instantaneous acceleration and vorticity magnitude at larval locations. Colors indicate magnitude of effect; some color-bar scales differ for larvae that swim vs. sink/dive. Colored polygons enclose 75% of co-occurring vorticity SD and acceleration SD in the water column of representative local *T. obsoleta* habitats (Delaware Bay, orange) and *T. trivittata* habitats (New Jersey shelf, red). Diagonal lines indicate co-occurring signals in isotropic turbulence.

Supporting Movie S1: *Tritia obsoleta* larva swimming in a petri dish. Video was recorded and played back at 10 frames per second. No length scale was recorded.

Supporting Movie S2: *Tritia trivittata* larvae swimming in a petri dish. Video was recorded and played back at 10 frames per second. No length scale was recorded.

References

[1] A. Stuart and J. K. Ord. *Kendall's Advanced Theory of Statistics, Volume 1, Distribution Theory.* Halsted Press, New York, 6th edition, 1994.

[2] S. A. Tabatabai. *Physical and biogeochemical modeling in Delaware Estuary.* Phd, Rutgers University, 2017.

[3] H. Tennekes and J. L. Lumley. *A First Course in Turbulence.* MIT Press, 1972.

[4] O. M. Phillips. *The Dynamics of the Upper Ocean.* Cambridge University Press, 1966.

[5] J. H. Trowbridge. On a technique for measurement of turbulent shear stress in the presence of surface waves. *J. Atmos. Ocean. Tech.*, 15:290–298, 1998.

[6] L. Umlauf and H. Burchard. A generic length-scale equation for geophysical turbulence models. *J. Mar. Res.*, 61:235–265, 2003.

[7] J. C. Warner, C. R. Sherwood, H. G. Arango, and R. P. Signell. Performance of four turbulence closure models implemented using a generic length scale method. *Ocean Model.*, 8:81–113, 2005.

[8] H. L. Fuchs and G. P. Gerbi. Seascape-level variation in turbulence- and wave-generated hydrodynamic signals experienced by plankton. *Progr. Oceanogr.*, 141:109–129, 2016.

[9] A. N. Kolmogorov. A refinement of previous hypotheses concerning the local structure of turbulence in a viscous incompressible fluid at high Reynolds number. *J. Fluid Mech.*, 13:82–85, 1962.

[10] H. L. Fuchs, E. J. Hunter, E. L. Schmitt, and R. A. Guazzo. Active downward propulsion by oyster larvae in turbulence. *J. Exp. Biol.*, 216:1458–1469, 2013.

[11] W. W. Rubey. Settling velocity of gravel, sand, and silt particles. *Am. J. Sci.*, 25:325–338, 1933.

[12] H. L. Fuchs, A. J. Christman, G. P. Gerbi, E. J. Hunter, and F. J. Diez. Directional flow sensing by passively stable larvae. *J. Exp. Biol.*, 218:2782–2792, 2015.

[13] H. L. Fuchs, G. P. Gerbi, E. J. Hunter, A. J. Christman, and F. J. Diez. Hydrodynamic sensing and behavior by oyster larvae in turbulence and waves. *J. Exp. Biol.*, 218:1419–1432, 2015.